Neogene Mantle Dynamics of Western Mediterranean Region Constrained by Basalt Geochemistry and Residual Depth Anomalies

Chia-Yu Tien*, Nicky White, John Maclennan, Benedict Conway-Jones, and Megan Holdt
Department of Earth Sciences, University of Cambridge, United Kingdom (cyt28@cam.ac.uk) **EGU23-434**

Sharing not permitted

1. Mantle Dynamics and Magmatism

- Dynamic topography and basaltic magmatism are consequences of mantle dynamics.
- Basalt geochemistry is used to constraint thermal structure of shallowest mantle.
- Correlations between Neogene magmatism, residual depth anomalies, and tomographic models.

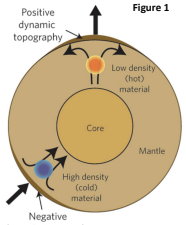

Figure 1

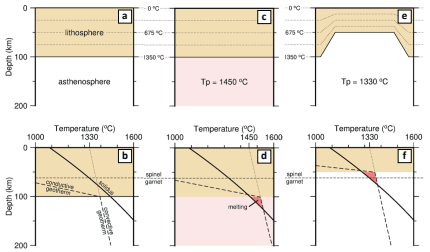

Figure 2

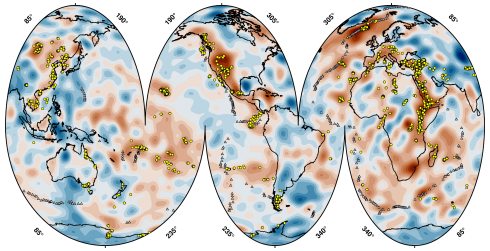

Figure 3

Figure 1: Cartoon showing dynamic topography caused by mantle upwelling and downwelling. Courtesy of J. Braun.

Figure 2: Cartoons illustrating two ways by which partial melting of dry mantle peridotite occurs. Thermal structure of: **(a), (b)** normal lithosphere and asthenosphere; **(c), (d)** abnormally hot asthenosphere; and **(e), (f)** abnormally thin lithosphere.

Figure 3: Observed dynamic topography (spherical harmonic degree 40; Holdt et al., 2022). Yellow circles are intraplate magmatic samples with age < 10 Ma from Ball et al. (2021). Gray triangles are ridge segments from Gale et al. (2013).

2. Western Mediterranean Region

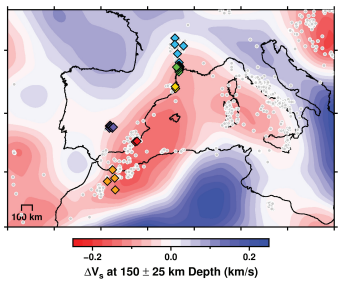

- Positive correlation between Neogene-Quaternary magmatism and slow shear-wave velocities.
- 50 basaltic samples located away from plate boundaries were collected, analysed and modelled.
- Samples filtered to identify primary melts from asthenospheric mantle.
  - volcanic rocks
  - 50 ≤ Mg# ≤ 80
  - $K_2O/Na_2O \leq 1$
  - $40 \leq SiO_2 \leq 56$ wt.%
  - $7.5 \leq MgO \leq 25$ wt.%
  - $(Nb/La)_{PC} \geq 1$

Figure 4: Shear-wave velocity anomalies averaged between 125 and 175 km from SL2013sv model (Schaeffer & Lebedev, 2013). Circles are published Neogene-Quaternary igneous samples from GEOROC and EarthChem databases. Coloured diamonds are basaltic rocks, including 50 collected samples, which pass our screening procedure (Carracedo-Sánchez et al., 2017; Cebriá et al., 2009; Dautria et al., 2010; Duggen et al. 2015; Liotard et al. 1995; Oeser et al. 2015). Red = SE Spain (Pliocene to Pleistocene); orange = N Morocco (Pliocene to Pleistocene); yellow = NE Spain (Pleistocene); green = S France (Pleistocene); blue = S France (Late Miocene to Early Pliocene); purple = Central Spain (Pliocene to Pleistocene).

3. Rare Earth Element (REE) Modelling

$$D = \frac{C_{source}}{C_{melt}}$$

- REEs have D < 1; F (T, P) is melt fraction; D (garnet in, spinel out).
- F (T, P) is inferred from observed C_{melt}, predetermined C_{source}, and D.
- Modelling yields potential temperature of 1275 °C & lithosphere of 70 km.

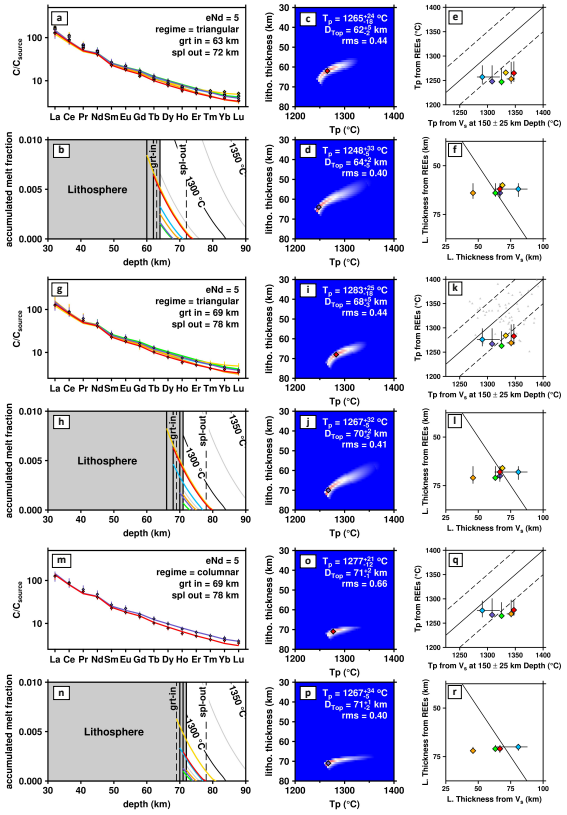

Figure 5: Adiabatic inverse modelling of REE concentrations. **(a)** REE concentrations normalised to source composition. Coloured diamonds and error bars = average observed REE concentrations ±σ; coloured lines = REE concentrations calculated by inverse modelling where rms values at global minima. **(b)** Melt fraction plotted as function of depth. Curved coloured lines = best-fitting melting paths; vertical black lines = best-fitting tops of melting columns; curved black/gray lines = adiabatic melting paths calculated using formulae and parameters from Katz et al. (2003) and Shorttle et al. (2014); vertical dash lines = spinel-garnet transition zone. **(c)** Misfit between observed and calculated REE concentrations plotted as function of asthenospheric potential temperature (T_P) and lithospheric thickness (D_{Top}) for SE Spain. Blue: rms > 1; white: rms = 1; red: rms < 1; coloured diamond = global minimum. **(d)** Same as (c) but for Central Spain. **(e)** Relationship between T_P determined by REE inversion of basalt geochemistry and that determined by temperature conversion of seismic tomographic model (McKenzie & O'Nions, 1991; Richards et al., 2020; Schaeffer & Lebedev, 2013). Black line = 1:1 relationship; dashed lines = ±25°C relationships. **(f)** Same as (e) but for D_{Top}. **(a-f)** Source is fixed with eNd = 5; triangular melting regime; spinel-garnet transition = 63-72 km from Jennings & Holland (2015). **(g-l)** Spinel-garnet transition = 69-78 km from Tomlinson & Holland (2021). Gray triangles = ridge segments from Gale et al. (2013). **(m-r)** Columnar melting regime.

4. Residual Depth Anomalies

- Residual depth anomalies match shear-wave velocity anomalies with maximum value of +1 km.

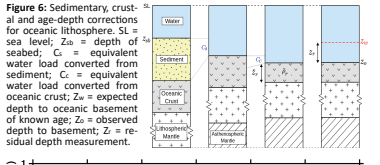

Figure 6: Sedimentary, crustal and age-depth corrections for oceanic lithosphere. SL = sea level; Z_{SB} = depth of seabed; C_E = equivalent water load converted from sediment; C_C = equivalent water load converted from oceanic crust; Z_M = expected depth to oceanic basement of known age; Z_O = observed depth to basement; Z_I = residual depth measurement.

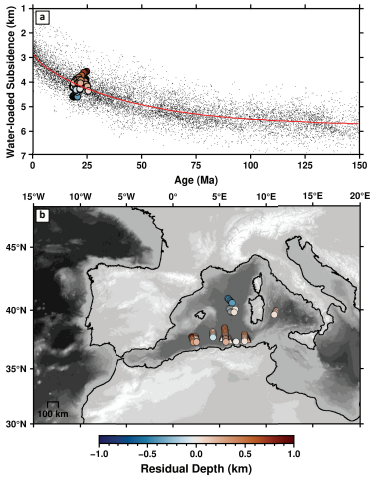

Figure 7: Residual depth anomalies. **(a)** Water-loaded depths to oceanic basement as function of plate age. Circles = measurements averaged within 0.1° bins; black dots = global measurements averaged within 1° bins; red line = plate model from Holdt et al. (2022). **(b)** Map of residual depth anomalies.

5. Dynamic Topographic Calculations

- Asthenospheric temperature is near ambient. Lithosphere is thin.
- Rayleigh wave velocity model implies ~70 km thick lithosphere.

$$U = \frac{\alpha T_1}{(1-\alpha T_1)}\left(\frac{a_1^2}{2a_0} + \frac{a_0}{2} - a_1 + \frac{\Delta T}{T_1}h\right)$$

- Thinning of 125 km lithosphere to 75 km generates 0.5 km of uplift.

U = amount of uplift
α = thermal expansivity
a_1 = initial thickness
a_0 = final thickness
T_1 = temperature
ΔT = thermal anomaly
h = thickness of anomaly

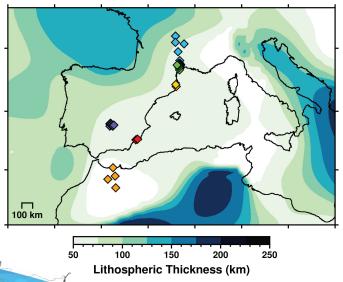

Figure 8: Lithospheric thickness calculated using 1175 °C isotherm converted from SL2013sv model using velocity temperature calibration scheme of Richards et al. (2020).

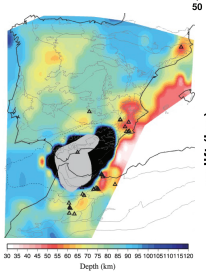

Figure 9: Lithospheric thickness inferred from Rayleigh wave phase velocity dispersion (Palomeras et al., 2017). Gray area = high velocity body at 90 km depth; black area = region where no LAB is detected; triangles = locations of volcanic rocks.

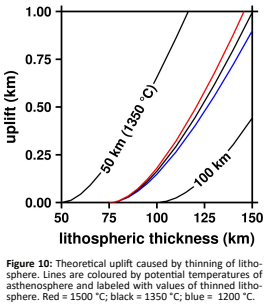

Figure 10: Theoretical uplift caused by thinning of lithosphere. Lines are coloured by potential temperatures of asthenosphere and labeled with values of thinned lithosphere. Red = 1500 °C; black = 1350 °C; blue = 1200 °C.

6. Independent Evidence for Regional Uplift

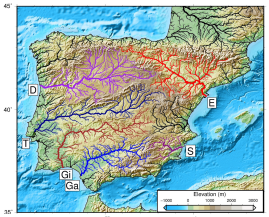

Figure 11

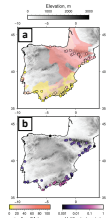

Figure 12

- Fluvial drainage flows away from slow shear-wave velocity anomaly.
- Neogene marine deposits from SE Spain imply uplift rates of ~0.05 mm/yr.
- Cumulative uplift inferred from calibrated drainage modelling is ~1 km.

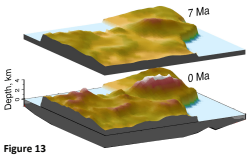

Figure 13

Figure 11: Iberian drainage patterns extracted from ASTER GDEM model by Conway-Jones et al. (2019). D = Duero; T = Tajo; Gi = Guadiana; Ga = Guadalquivir; S = Segura; E = Ebro.

Figure 12: Iberian biostratigraphic constraints compiled by Conway-Jones et al. (2019) **(a)** Marine and coastal stratigraphy coloured by age. Circles = Cenozoic marine fossils recorded in PaleoDB database. Triangles = radiometric ages of marine terraces. **(b)** Calculated average uplift rates.

Figure 13: Calculated cumulative uplift.